CrossMark

Congo red decomposition by photocatalytic formation of hydroxyl radicals ('OH) using titanium metal–organic frameworks

Nelson J. Castellanos[1] [ORCID] · Zulied Martinez Rojas[1] · Hernando A. Camargo[2] · Shyam Biswas[3] · Gilma Granados-Oliveros[4]

Abstract

In this work, two well-known titanium-type metal–organic framework (MOF) solids named MIL-125 and MIL-125-NH$_2$ were successfully synthesized using a solvothermal method. The structure of the catalytic materials was confirmed by X-ray powder diffraction, infrared spectroscopy, N$_2$ adsorption–desorption measurements, thermogravimetric analysis and UV–Vis diffuse reflectance spectroscopy analysis. An azo dye, Congo red, was used as model pollutant to study its photocatalytic activity under UV–Vis light irradiation. A comparison with the commercial TiO$_2$ P-25 revealed both the beneficial effect of the porous structure of MOFs and the influence of the –NH$_2$ group on the light activation process. Formation of hydroxyl radicals ('OH) by catalysts was evaluated by luminol degradation probing. Finally, the titanium MOF catalysts can be recycled and reused without significant loss of activity.

Introduction

Azo dyes are currently one of the families of organic compounds with the greatest environmental impact [1, 2]. They represent more than 60% of the commercial dyes used in the textile, food, pharmaceutical, paper and ink industries, which are generally discharged to the environment in wastewater from industrial processes [3, 4]. The biological effects of this wastewater are associated with a low biological oxygen demand (BOD) and a high chemical oxygen demand (COD) which leads to serious damage to aquatic life (fauna and flora) [5, 6]. To reduce these negative agents, different removal or decomposition treatment methodologies have been proposed, such as the use of ultrasonic processing [7], the treatment of activated sludges [8], catalytic oxidation [9], or simple physisorption [10, 11]. Although some of them have been proven to be successful and reduce concentration, the challenge is currently focused on designing new solid materials than can be recovered and reused for better removal or disposal, and working under green chemistry conditions, using alternative energy sources such as sunlight [12, 13].

In this way, recently metal–organic frameworks (MOFs) have emerged as a new class of porous solid materials. In these solids, the metal centers mainly correspond to divalent and trivalent ions of 3d transition metals (Zn, Cu, Fe, Ni, etc.), 3p or lanthanoid metals bound to organic molecules through –COOH groups in particular, obtaining solid structures with stable and specific topologies characterized by crystalline structures, large specific surface area, high pore volume and structural adaptivity [14–16].

MOFs have potential applications in gas storage, separation and adsorption of molecules, catalysis, thin films, magnetism, or the administration of drugs in living organisms [17]. For applications in catalysis, MOFs have some advantages compared to zeolites, because they do not require activation or regeneration at high temperatures [18, 19]. In addition, MOFs behave as semiconductors when exposed to light and can undergo charge separation upon light absorption [20, 21],

✉ Nelson J. Castellanos
  njcastellanosm@unal.edu.co

1 Estado Sólido y Catálisis Ambiental (ESCA), Department of Chemistry, Faculty of Science, Universidad Nacional de Colombia, Carrera 30 No. 45-03, Bogotá, Colombia
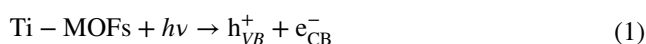
2 Grupo de Investigación en Nuevos Materiales y Energías Alternativas (GINMEA), Facultad de Química Ambiental, Universidad Santo Tomás, Campus Universitario Floridablanca, Santander, Colombia

3 Department of Chemistry, Indian Institute of Technology Guwahati, Guwahati, Assam 781039, India

4 Nuevos Materiales Nano y Supramoleculares, Department of Chemistry, Faculty of Science, Universidad Nacional de Colombia, Carrera 30 No. 45-03, Bogotá, Colombia

thus finding applications in different fields of interest such as solar-fuels production [22, 23], photovoltaic and light-emitting devices [24, 25], photocatalytic transformations such as CO_2 reduction [26] and photocatalysis for pollutant degradation [27–29].

In this context, the photocatalytic process initiates when the semiconductor surface is irradiated with photons whose energy is equal to or greater than the energy gap between its bands, energy-rich electron–hole pairs are formed on its surface (reaction 1). Photogenerated holes (h_{VB}^+) react with water (reaction 2) and electrons (e_{CB}^-) with oxygen (reaction 3) to form reactive oxygen species (ROS) such as hydroxyl radicals ($\cdot$OH) and superoxide radical anions ($O_2^{\cdot-}$). Specifically, $\cdot$OH radicals are powerful oxidizing species in aqueous media with notable reactivity toward a wide variety of aromatic pollutants to achieve mineralization.

$$Ti - MOFs + h\nu \rightarrow h_{VB}^+ + e_{CB}^- \tag{1}$$

$$h^+ + H_2O \rightarrow \cdot OH + H^+ \tag{2}$$

$$e^- + O_2 \rightarrow O_2^{\cdot-} \tag{3}$$

Although some examples of photocatalytic degradation of pollutants using MOFs have been reported in the literature, species that participate in the degradation process are not usually identified. For example, photodegradation of diclofenac and methylene blue has been performed in the presence of MIL-53 [30]. MOF-5 has been used as a microporous semiconductor for carrying out a study of the photocatalytic degradation of phenol in aqueous solutions [21]. Aqueous Cr(VI) photocatalytic reduction was performed in the presence of NNU-36 [31]. The photocatalytic behavior of MIL-100(Fe) was evaluated in the degradation of photocatalytic methyl orange in water [32].

In this context, the aim of this work was to study the catalytic activity of two solid titanium MOFs in photodegradation reactions of pollutants in aqueous phase at room temperature and atmospheric pressure. MIL-125 and MIL-125-NH$_2$ were studied due to their promising electronic and photocatalytic properties, high thermal and chemical stability and unique structural characteristics [33]. Congo red dye was used as a model molecule to explore the photocatalytic properties of these solids [34, 35], and reactive oxygen species $O_2^{\cdot-}$ and $\cdot$OH were identified by measurements of luminol chemiluminescence reactions [36]. Finally, the titanium MOF catalysts were recycled and reused without significant loss of activity. The development and knowledge of a stable photoactive system for degradation of emerging contaminants contribute to the development of sustainable technologies based on the use of solar energy to activate the catalyst, and recoverable and reusable solid materials topics.

Experimental

All chemicals were purchased from Sigma-Aldrich or Alfa Aesar and used without further purification. Commercial grade solvents were dried and deoxygenated by refluxing for at least 12 h over appropriate drying agents under argon atmosphere and were freshly distilled prior to use. X-ray powder diffraction (XRPD) analyses of solid titanium MOFs were performed in an X'Pert Pro MPD PANalytical instrument with a Cu anode (Cu Kα radiation, $\lambda = 1.54056$ Å) using a Bragg–Brentano configuration. Diffractograms of the powder samples were recorded at room temperature, with step size of 0.02 2θ and 10 s step time. The FT-IR ATR spectra were obtained with a Shimadzu IR prestige 21 spectrophotometer (Columbia, MD, USA). Nitrogen adsorption–desorption measurements were taken at -196 °C on a Micromeritics ASAP 2010 adsorption analyzer to determine the Langmuir surface area. Before measurement, samples were evacuated for 12 h at 110 °C and 1 μtorr [37]. Pore volume was determined by applying the Dubinin–Astakhov (D–A) method, and the pore size was calculated using the Horvath–Kavazoe (HK) method [38, 39]. Diffuse reflectance UV–Vis spectra of solid samples were recorded on a Hitachi U-3000 UV–Vis spectrophotometer. The irradiation intensity of the halogen lamp used in photochemical experiments was measured by a Hand-Held Optical Power Meter Model 840-C, and the photon flux emission corresponded to 85 mW cm^{-2} at 390 nm. Band gap energy (E_g) of the photocatalysts was calculated from their diffuse reflectance UV–Vis spectra according to the Kubelka–Munk theory [40]. The band gap was obtained from a plot of $[F(R\infty)\cdot E]^{1/2}$ versus energy of the exciting light (E) assuming that titanium MOFs are indirect crystalline semiconductors [41].

Synthesis and characterization of MOFs

Synthesis of MIL-125 (1)

MIL-125 or Ti$_8$O$_8$(OH)$_4$[O$_2$C–C$_6$H$_4$–CO$_2$]$_6$ was synthesized following a previously published procedure [42, 43] using terephthalic acid (TA) (0.5 g, 3 mmol) and titanium isopropoxide Ti(OiPr)$_4$ (0.6 mL, 1.5 mmol) in a solution of 9 mL of N,N-dimethylformamide (DMF) and 0.5 mL of dry methanol. The mixture was stirred gently for 5 min at room temperature and then placed within a 25-mL Teflon liner and heated at 150 °C for 16 h. After reaction, the resultant suspension was filtered, washed with DMF and methanol, respectively, and dried at 150 °C under vacuum overnight to obtain a white solid product. FT-IR ATR (cm^{-1}): 1535, 1512 (–COO asymmetrical vibration); 1390 (–COO symmetrical vibration).

Synthesis of MIL-125-NH$_2$ (2)

MIL-125-NH$_2$ was synthesized by using a solvothermal method that is based on the preparation of MIL-125 previously reported by Dan-Hardi [43, 44], except that TA was replaced by 2-aminoterephthalic acid (NH$_2$–TA) and the solvothermal time was 60 h. FT-IR ATR (cm^{-1}): 1571, 1496 (–COO asymmetrical vibration); 1386 (–COO symmetrical vibration); 1531 (N–H deformations); 1421 (CN vibrations).

Photocatalytic degradation of Congo red

Photocatalytic degradation of Congo red (CR) was studied using a 100-ppm solution of CR in the presence of 150 mg of catalyst, maintaining a ratio of 1 mg of catalyst/mL of solution. The reaction was carried out under stirring and constant irradiation for 3 h using a batch photochemical reactor equipped with an immersion lamp (Phenix, 220 V, 150 W, $\lambda > 390$ nm). Follow-up of the degradation of azo dye pollutant was performed by calculating the concentration of Congo red by UV–visible spectroscopy (HP-8453) following the maximum absorption band at 498 nm. In a typical experiment, 1 mL reaction aliquots were taken every 30 min, which were centrifuged and their concentration compared to the calibration curve previously obtained with aqueous solutions of Congo red, using a concentration range of 100–2 ppm. In order to assess the role of dissolved O$_2$, N$_2$ was bubbled into catalyst aqueous suspensions for 1 h before irradiation and N$_2$ atmosphere was maintained during photocatalytic reaction. Control experiments were performed in darkness conditions and in the absence of catalyst but under irradiation.

Degradation of luminol

To evidence the formation of ROS from catalyst suspensions, the degradation of luminol was carried out by adding 20 mg of catalyst to 20 mL of luminol aqueous solution (2.7 mmol, pH 7). The suspension was stirred in the dark for 1 h before irradiating, and O$_2$ was bubbled through the suspension. The reaction mixture was irradiated with a Sylvania 125 W mercury lamp equipped with an optical filter S-8022 SCHOTT ($\lambda_{\text{transmitted}} > 360$ nm). The incident light flux (I_o) was measured by actinometry of potassium ferrioxalate, K$_3$Fe(C$_2$O$_4$)$_3$·3H$_2$O, ($I_o = 1.5 \times 10^{-5}$ mol L^{-1} s^{-1}) [45, 46]. The reactions were performed at 25 °C. Aliquots of 0.2 mL were collected during irradiation, which were then centrifuged and quantified with luminol fluorescence at 431 nm. (Excitation wavelength was 405 nm.) Measurements of luminol fluorescence were taken with a Vernier SpectroVIS Plus spectrofluorometer. The concentration of luminol was compared from fluorescence intensity of a luminol solution of known concentration. Identification of

reactive species was carried out in the presence of radical scavengers: Hydroxyl radicals (˙OH) was verified by adding 100 μL of 0.1 M mannitol solution (a scavenger of ˙OH [47, 48]) to the suspension before irradiation. Degradation of luminol was also carried out under visible irradiation by using a 50 W white LED (Philips, $\lambda > 420$ nm), and I_o was 8.4×10^{-5} mol L^{-1} s^{-1} determined by Reinecke salt actinometry [49]. The experimental conditions under visible irradiation were the same as in UV irradiation experiments.

Results and discussion

Preparation of the catalyst

MIL-125 and MIL-125-NH$_2$ solids have been synthesized by solvothermal method similar to a reported procedure [43]. This method employs anhydrous titanium isopropoxide, aromatic ligands substituted with carboxylic groups and a suitable solvent mixture (in this case, DMF and CH$_3$OH) which favors the interaction between metal and the carboxylic groups of the ligand at 150 °C. Since the crystallinity, surface and structural characteristics of titanium MOFs are affected by the presence of traces of water, extra-dry solvents (previously distilled) and fully controlled reaction conditions must be employed to obtain solids with reproducible results [50].

Characterization of Ti-MOFs

Figure 1 shows the XRPD patterns of MIL-125 and MIL-125-NH$_2$ solids prepared by solvothermal method. The strong and sharp diffraction peaks indicate good crystallinity of samples. These patterns are in accord with the University of Cambridge database: MIL-125 (cif-file CCDC 75115) and MIL-125-NH$_2$ (cif-file COD 7211159) [43]. The indexing of the peaks was done considering a tetragonal unit cell
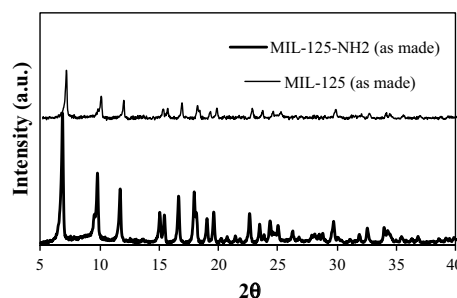

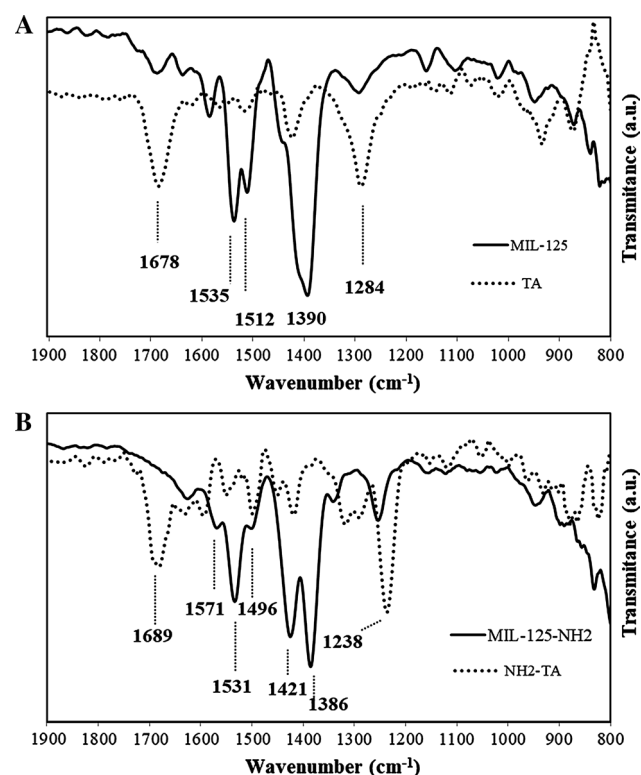**Fig. 1** XRD patterns of MIL-125 and MIL-125-NH2 solids

Table 1 Cell parameters obtained of MIL-125 and MIL-125 NH$_2$

Space group	MIL-125 I$_4$/MMM	MIL-125-NH$_2$ I$_4$/MMM
a (Å)	18.23	18.38
b (Å)	18.23	18.38
c (Å)	18.24	18.00
α	90°	90°
β	90°	90°
γ	90°	90°

with spatial group I$_4$/MMM, and the cell parameters are presented in Table 1.

No changes in the crystal lattice structure of MIL-125 were observed with the presence of –NH$_2$ group of the organic linker.
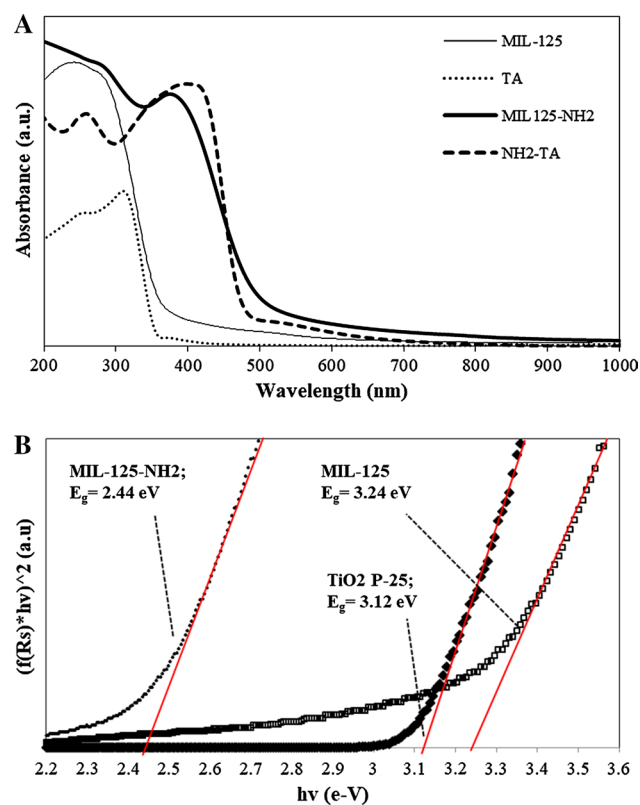
Figure 2 shows the FT-IR ATR spectra of MIL-125 and MIL-125-NH$_2$ in comparison with their respective dicarboxylic acid ligands. Typical signals for MIL-125 were exhibited at (in cm^{-1}) 1535 (N–H deformation), 1512 (–COO asymmetrical vibration) and 1390 (–COO symmetrical vibration), whilst for MIL-125-NH$_2$, the signals were observed at (in cm^{-1}) 1531 (N–H deformations), 1421 (CN vibrations), 1571 and 1496 (–COO asymmetrical vibration) and 1386 (–COO symmetrical vibration) [51].

The R-COOH functional group bands of the starting ligands underwent major changes after complexation with Ti(IV) leading to the formation of MIL-125 and MIL-125-NH$_2$ solids. In this case, the disappearance of the carbonyl group (C=O) band (at 1678 cm^{-1} for TA and 1689 cm^{-1} for NH$_2$–TA) and the formation of two new bands at 1600–1500 cm^{-1} and 1450–1350 cm^{-1} could be appreciated, corresponding to asymmetrical and symmetrical stretching of the carboxylate group (COO$^-$), respectively [50]. Thus, interaction between Ti(IV) and –COOH functional group of ligands could induce a resonance structure of carboxylate group (–COO). These results provide evidence for the successful complexation and formation of titanium MOFs.

Figure 3a compares the diffuse reflectance UV–Vis spectra of titanium MOFs with their respective starting ligands in solid state. The characteristic absorption bands of the ligands correspond to $n \rightarrow \pi^*$ (246 nm for TA and 255 nm for NH$_2$–TA) and $\pi \rightarrow \pi^*$ (306 nm for TA, 402 nm for NH$_2$–TA) electronic transition [36, 52]. Owing to their

Fig. 2 FT-IR spectra of **a** MIL-125 and **b** MIL-125-NH$_2$ (solid line) in comparison with their respective ligands (dashed line)

Fig. 3 **a** UV–Vis diffuse reflectance spectra of MIL-125 and MIL-125-NH$_2$ (solid line) in comparison with their respective ligands (dashed line). **b** Band gap plot of MIL-125 and MIL-125-NH$_2$ calculated from their diffuse reflectance UV–Vis spectra. A comparison with TiO$_2$ P-25 is presented as reference material

semiconducting properties, broader and less defined bands have been observed in the UV–Vis spectra for MIL-125 and MIL-125-NH$_2$. MIL-125-NH$_2$ exhibits an obvious redshift in the absorption bands and higher absorption above 350 nm than that of MIL-125. These changes indicate the influence of –NH$_2$ groups on the electronic band structure of titanium MOFs [44].

Band gap energies (E_g) of MIL-125 and MIL-125-NH$_2$ were calculated from diffuse reflectance UV–Vis spectra according to the Kubelka–Munk theory [53] and were compared to that obtained for TiO$_2$ P-25, which was used as the reference material (Fig. 3b) [54, 55]. The experimental value of E_g for TiO$_2$ P-25 was 3.12 eV and matches well with the reported values in the literature [56]. The E_g values for MIL-125 and MIL-125-NH$_2$ solids were 3.24 eV and 2.44 eV, respectively. According to their semiconducting properties, MIL-125-NH$_2$ can be activated under visible light irradiating in contrast to TiO$_2$ and MIL-125 which require of UVA light (< 390 nm) to initiate the photocatalytic process.

The surface features of the synthesized titanium MOFs were investigated by applying Langmuir model to the N$_2$ adsorption/desorption isotherms measured at 77 K. The results are summarized in Table 2. The experimental sorption isotherms are shown in Fig. 4a. According to IUPAC classification, MIL-125 shows a type-Ia isotherm which is typically found for microporous structures. On the other hand, MIL-125-NH$_2$ exhibits type-Ib. Type-Ib isotherms are characteristic of materials having pore size distributions in a wide range, ranging from wider micropores to narrow mesopores [37].

The prepared titanium MOFs showed high surface areas. The values of surface areas correspond to 635 m^2 g^{-1} for MIL-125 and 902 m^2 g^{-1} for MIL-125-NH$_2$, in contrast with the low area of TiO$_2$ (50 m^2 g^{-1}). The pore volume was estimated using the Dubinin–Astakhov method, which is based on the linearization of the adsorption isotherms (Fig. 4b). Thus, pore volume was 0.35 cm^3 g^{-1} for MIL-125 and 0.46 cm^3 g^{-1} for MIL-125-NH$_2$. A deviation from linearity was observed at both lower and higher pressures, which corroborates a microporous surface [57]. Likewise, when the pore size distribution was plotted by the Horvarth–Kawazoe

Table 2 N$_2$ adsorption–desorption measurements for MIL-125 and MIL-125-NH$_2$

Catalyst	Langmuir surface area (m^2/g)	Pore volume[b] (cm^3/g)	Pore size[a] (nm)
MIL-125	635	0.35	0.80
MIL-125-NH$_2$	902	0.46	0.83

[a]The pore size was calculated using the Horvath–Kavazoe (HK) method

[b]The pore size was calculated applying the Dubinin–Astakhov (D–A) method
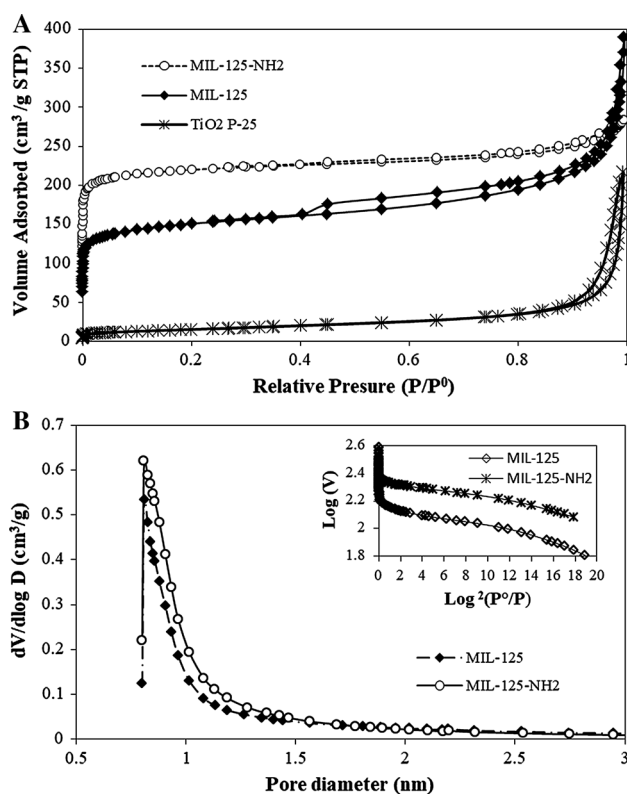
Fig. 4 a Nitrogen adsorption–desorption isotherms and **b** corresponding pore size distribution curves of MIL-125 and MIL-125-NH$_2$ solids

(HK) method, which is the analytical method used for microporous structures [58], a monomodal distribution with diameters of 0.80 and 0.83 nm was obtained for MIL-125 and MIL-125-NH$_2$, respectively.

Photocatalytic degradation of Congo red

Figure 5 compares the results obtained from the removal capacity of the Congo red dye by MIL-125 and MIL-125-NH$_2$ by physical adsorption on the surface of each of the solids. The MIL-125 solid achieved 20% dye removal by adsorption, while a slight increase was obtained for MIL-125-NH$_2$ with 24% adsorption. This greater increase in the removal is associated with the surface polarization of the solid induced by the –NH$_2$ groups of the ligand in the MIL-125-NH$_2$ catalyst [59]. In the case of TiO$_2$ P-25, the adsorption capacity of the dye did not exceed 10%.

Figure 6a shows the photocatalytic degradation of Congo red by MIL-125, MIL-125-NH$_2$ and TiO$_2$ P-25 (which was used as reference photocatalyst) in oxygenated aqueous suspensions and under UVA light irradiation ($\lambda > 390$ nm). Although all catalysts were able to achieve Congo red degradation, MIL-125-NH$_2$ showed higher photoactivity and a substantial degradation (97%) after 3 h of irradiation. In
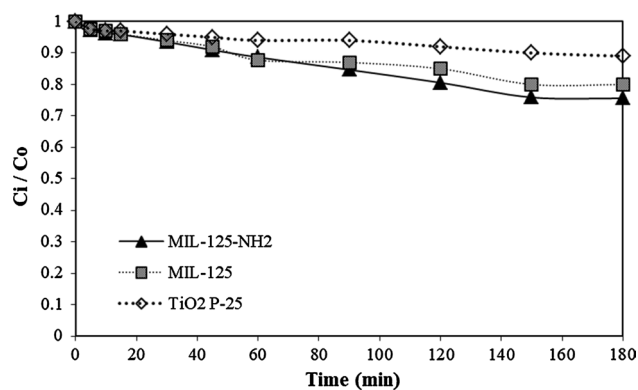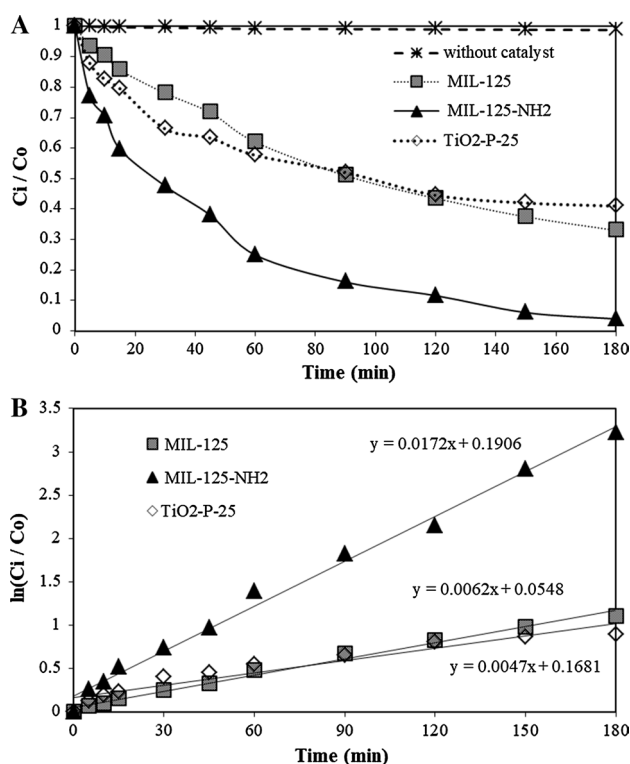
Fig. 5 Comparison of the concentration change in the adsorption process by MIL-125, MIL-125-NH$_2$ and TiO$_2$ P-25

contrast, the dye degradation was around 60% with MIL-125 and TiO$_2$ P-25. Control experiments were also carried out, and the direct photolysis of the azo dye was negligible.

Photodegradation on a catalyst surface can be expressed by the Langmuir–Hinshelwood model and follows a pseudo-first-order kinetics with respect to dye concentration [60]:
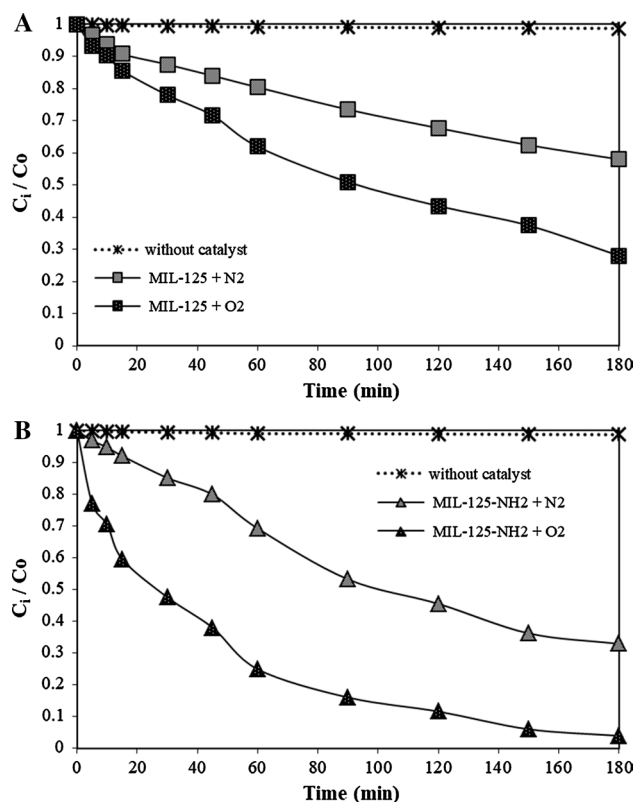
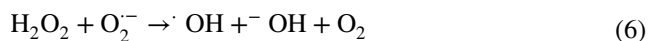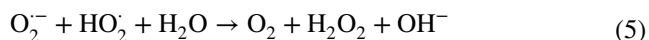$$-\ln(C_{i}/C_0) = K_{app}t \qquad (4)$$

where C_i and C_0 are the dye concentration at time $t = t$ and $t = 0$, respectively; K_{app} is the apparent reaction rate constant; and t is time. K_{app} was obtained from the slope of a $\ln(C_i/C_0)$ versus t plot (Fig. 6b) and was higher for MIL-125-NH$_2$ ($K_{app} = 0.0175$ min^{-1}) followed by MIL-125 ($K_{app} = 0.0062$ min^{-1}). These new photocatalysts showed faster kinetics than TiO$_2$ P25 ($K_{app} = 0.0047$ min^{-1}) which has been typically used in degradation processes with important results. We highlight the fact that MIL-125-NH$_2$ with higher surface area could have more catalytic surface sites to accelerate the reaction. Metal ions of the MOF can act as Lewis acid sites to coordinate Congo red that is then removed [61].

Figure 7 shows the effect of oxygen in the azo dye photodegradation by Ti-MOFs. In this case, N$_2$ was bubbled through the suspension to remove dissolved oxygen from solution and Congo red degradation kinetics were investigated. In these conditions, degradation was 67% with MIL-125-NH$_2$ and 42% with MIL-125, revealing that molecular O$_2$ is required to achieve the advanced oxidation more quickly. Additionally, O$_2$ is indispensable to trap e$_{CB}^-$ generated after excitation of Ti–MOFs and also to avoid the undesirable recombination of h$_{VB}^+$/e$_{CB}^-$ pairs. Additionally, oxygen could be considered as a green oxidizing agent since

Fig. 6 a Degradation of Congo red as a function of irradiation time for MIL-125 and MIL-125-NH$_2$ and TiO$_2$ P-25 catalysts. **b** Linearization of Congo red degradation (ln C_i/C_0 vs. irradiation time)


Fig. 7 Analysis of O$_2$ bubbling in the photocatalytic degradation of Congo red by comparison of change in concentration of CR as a function of irradiation time: **a** MIL-125 and **b** MIL-125-NH$_2$

it is the predominant reactant able to generate ROS, such as $O_2^{.-}$ and $^.OH$, according to reactions 2 and 3. However, the radical $O_2^{.-}$ (pKa = 4.88) could undergo dismutation to generate hydrogen peroxide (reaction 5) which is finally reduced to $^.OH$, according to reactions 6–7 [62–64]. Therefore, $^.OH$ could be considered as the main intermediate formed by MIL-125 and MIL-125-NH$_2$ during the photocatalytic degradation process of Congo red.

$$O_2^{.-} + HO_2^. + H_2O \rightarrow O_2 + H_2O_2 + OH^- \qquad (5)$$

$$H_2O_2 + O_2^{.-} \rightarrow\ ^.OH +^- OH + O_2 \qquad (6)$$

$$H_2O_2 + e_{CB}^- \rightarrow\ ^.OH +^- OH \qquad (7)$$

Thus, with the aim of investigating the reactivity of titanium MOF materials and their ability to produce hydroxyl radicals, a luminol degradation test was carried out. Luminol could be selectively degraded by $O_2^{.-}$ and $^.OH$. The facile disproportionation reaction of superoxide in water (reactions 6–7) precludes the reaction between $O_2^{.-}$ and luminol. Thus, we assume that the $^.OH$ radicals are mainly responsible for the luminol degradation [65].
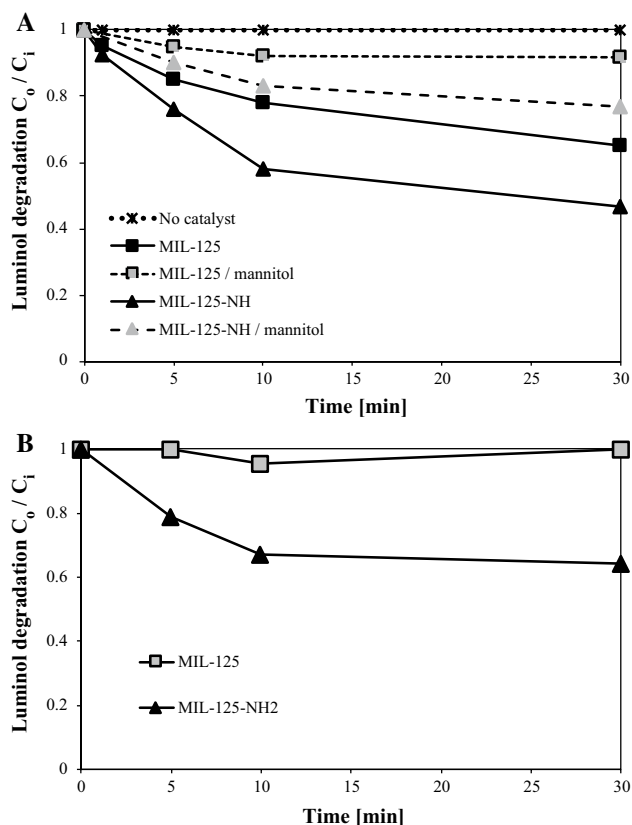
Fig. 8 Luminol degradation by MIL-125 and MIL-125-NH$_2$ in oxygenated aqueous suspensions, at room temperature, under **a** UV irradiation ($\lambda > 360$ nm) and **b** visible irradiation ($\lambda > 420$ nm)

Table 3 K_{app} values obtained of MIL-125 and MIL-125 NH$_2$ in luminol degradation

Catalyst	K_{app} (min^{-1}) UV ($\lambda > 360$ nm)	K_{app} (min^{-1}) Vis ($\lambda > 420$ nm)
MIL-125-NH$_2$	0.053	0.040
MIL-125	0.024	No degradation

Figure 8a shows luminol degradation by MIL-125 and MIL-125-NH$_2$ in oxygenated aqueous suspensions, at room temperature, under UV ($\lambda > 360$ nm) irradiation. After irradiating for 1 h, luminol was degraded by up to 54% for MIL-125-NH$_2$ and 34% for MIL-125. No degradation was observed when the experiment was performed in the dark as well as on the experiments realized without catalyst. Since luminol degradation could be mainly carried out by $^.OH$, the participation of these species was evidenced by the effect of mannitol, a known $^.OH$ scavenger, into the titanium MOF dispersions. In these conditions, the degradation was only 8.3% for MIL-125 and 23% for MIL-125-NH$_2$, confirming that $^.OH$ radicals are formed by the titanium MOFs (Fig. 8a). The decay of luminol concentration could be fitted to the kinetic model of pseudo-first order (Eq. 1) to estimate K_{app} for the photocatalysts (Table 3). The value of K_{app} for MIL-125-NH$_2$ was 0.053 min^{-1}, while for MIL-125 it was 0.024 min^{-1}. These values clearly indicate that the degradation rate depends on the type of material used.

The production of hydroxyl radicals as well as adsorption of Congo red on the catalyst surface plays an important role in the photocatalytic process. In turn, the adsorption can limit the rate and efficiency of the total reaction. In this case, we hypothesize that NH$_2$-modified MOF has more active sites, which increases the adsorption capacity of organic molecules and accelerates the formation of $^.OH$ radicals. In contrast, the surface of MIL-125 exhibits weak interaction with Congo red and slower kinetics of $^.OH$ formation. The Congo red elimination depends principally on the production of $^.OH$ radicals and/or adsorption on catalyst surface, as a prerequisite for its oxidation. The luminol degradation experiments demonstrated that these new photocatalysts, MIL-125-NH$_2$ and MIL-125 MOF, in the presence of O$_2$ and upon UV light irradiation, are capable of producing hydroxyl radicals, which are powerful oxidants.

On the other hand, we have found that the introduction of –NH$_2$ groups into the MOFs induces changes in the band structure, producing shifts in band gap energy values at longer wavelengths. In this context, we have also evaluated the formation of $^.OH$ under visible irradiation ($\lambda > 420$ nm) (Fig. 8b). The degradation of luminol could be carried out by MIL-125-NH$_2$ with $K_{app} = 0.040$ min^{-1} (see Table 3). In contrast, MIL-125 was not able to perform the luminol degradation, which indicates that the photocatalytic process

was not initiated and no $^{\cdot}$OH radicals could be formed. Since one of the most interesting features of photocatalysis is the possibility of using solar light which corresponds to 95% of visible radiation, MIL-125-NH$_2$ is a new option to be used in environmental applications. This photocatalyst along with O$_2$ and visible light would notably reduce the economic cost of the technique and make it more sustainable.

Recyclability of MIL-125 and MIL-125-NH$_2$

In order to evaluate the stability of MIL-125 and MIL-125-NH$_2$ during the photodegradation of Congo red, the solid catalysts were separated from the reaction medium by filtration after a catalytic run for 180 min, consequently washed with water and acetone, and finally dried in vacuum. These used solids were characterized by IR and UV–Vis DRS spectroscopy and TGA (see Fig. 9).

The IR spectra of the used solids in the range 800–1900 cm^{-1} exhibit bands due to stretching vibrations of the titanium-organic frameworks that are identical to those of the precursor MIL-125 and MIL-125-NH$_2$ before catalysis. Furthermore, both thermogravimetric and XRPD analyses of the used MOF catalysts (Fig. 10) corroborate the structural integrity of the titanium MOFs. Thus, the structures of organic dicarboxylic acid ligands of the catalysts are
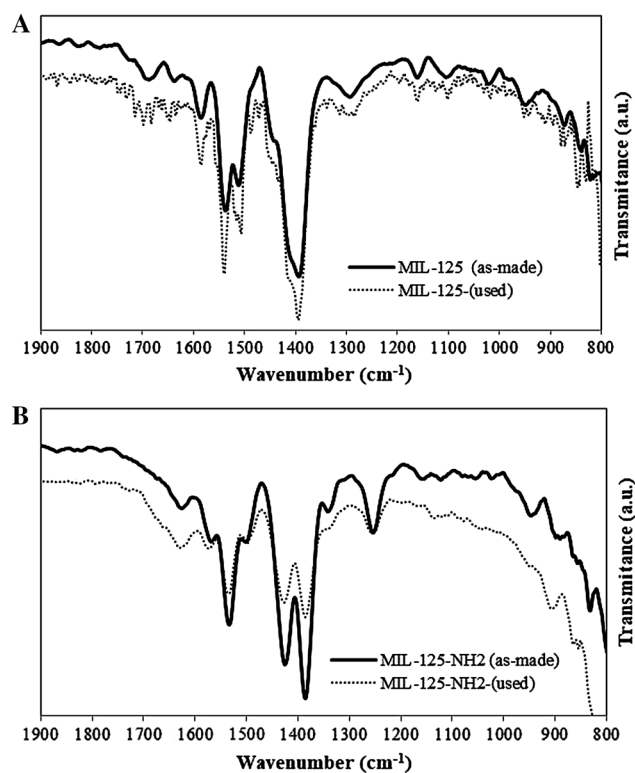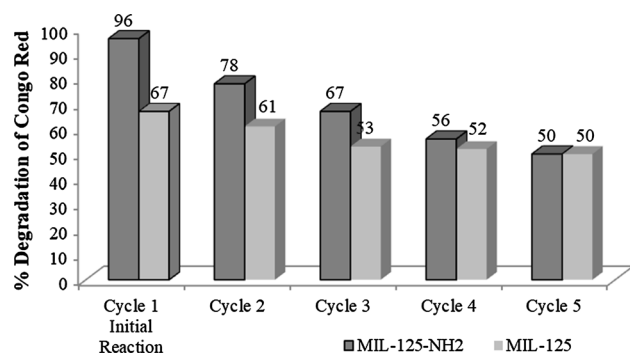
Fig. 9 FT-IR spectra for as-made and used **a** MIL-125 and **b** MIL-125-NH$_2$ catalysis texted in photocatalytic degradation of Congo red
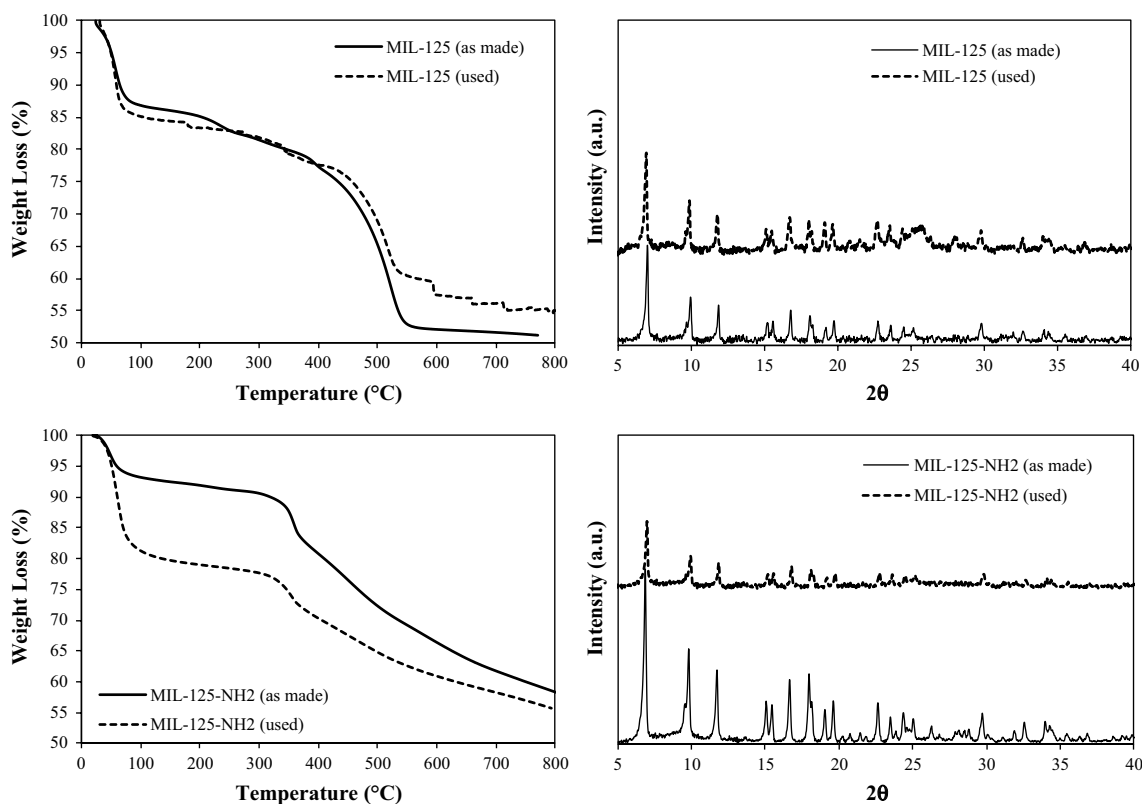
Fig. 10 TGA and XRPD analysis for as-made and used MIL-125 and MIL-125-NH$_2$ catalysis

Fig. 11 Percentage degradation of Congo red in different catalytic runs by MIL-125 and MIL-125-NH$_2$

not affected by the reactive oxygen species generated in the photocatalytic process.

In addition, to ascertain the reusability of the heterogeneous catalysts during the photodegradation reaction, each catalyst was tested over four additional catalytic runs.

Interestingly, as shown in Fig. 11, the catalytic activity is preserved, with a slight reduction in the photodegradation rate of Congo red from cycle to cycle. The results suggest that both MIL-125 and MIL-125-NH$_2$ have good potential as catalysts to be used and recycled in photodegradation processes.

Conclusions

In this paper, we have demonstrated that the MIL-125 and MIL-125-NH$_2$ solids are photoactive catalysts that participate in the photoformation of reactive oxygen species. The Ti-MOF catalysts evaluated have shown the activation of molecular O$_2$ in the decomposition processes of emerging pollutant molecules such as Congo red and have demonstrated their ability to be recycled and reused with only a small reduction in their photocatalytic activity. The proposed methodology has been proven to be a green alternative for the implementation of a photocatalytic process for water removal or decontamination, simply by the use of light and molecular O$_2$.

References

1. Rawat D, Mishra V, Sharma RS (2016) Detoxification of azo dyes in the context of environmental processes. Chemosphere 155:591–605. https://doi.org/10.1016/J.CHEMOSPHERE.2016.04.068

2. Kant R (2012) Textile dyeing industry an environmental hazard. Nat Sci 04:22–26. https://doi.org/10.4236/ns.2012.41004

3. Erdemoğlu S, Aksu SK, Sayılkan F et al (2008) Photocatalytic degradation of Congo Red by hydrothermally synthesized nanocrystalline TiO$_2$ and identification of degradation products by LC–MS. J Hazard Mater 155:469–476. https://doi.org/10.1016/J.JHAZMAT.2007.11.087

4. Saini RD (2017) Textile organic dyes: polluting effects and elimination methods from textile waste water. Int J Chem Eng Res 9:975–6442

5. Brüschweiler BJ, Merlot C (2017) Azo dyes in clothing textiles can be cleaved into a series of mutagenic aromatic amines which are not regulated yet. Regul Toxicol Pharmacol 88:214–226. https://doi.org/10.1016/J.YRTPH.2017.06.012

6. Stingley RL, Zou W, Heinze TM et al (2010) Metabolism of azo dyes by human skin microbiota. J Med Microbiol 59:108–114. https://doi.org/10.1099/jmm.0.012617-0

7. Das R, Bhaumik M, Giri S, Maity A (2017) Sonocatalytic rapid degradation of Congo red dye from aqueous solution using magnetic Fe0/polyaniline nanofibers. Ultrason Sonochem 37:600–613. https://doi.org/10.1016/J.ULTSONCH.2017.02.022

8. Ning X, Yang C, Wang Y et al (2014) Decolorization and biodegradation of the azo dye Congo red by an isolated Acinetobacter baumannii YNWH 226. Biotechnol Bioprocess Eng 19:687–695. https://doi.org/10.1007/s12257-013-0729-y

9. Yuan G-E, Li Y, Lv J et al (2017) Integration of microbial fuel cell and catalytic oxidation reactor with iron phthalocyanine catalyst for Congo red degradation. Biochem Eng J 120:118–124. https://doi.org/10.1016/J.BEJ.2017.01.005

10. Srilakshmi C, Saraf R (2016) Ag-doped hydroxyapatite as efficient adsorbent for removal of Congo red dye from aqueous solution: synthesis, kinetic and equilibrium adsorption isotherm analysis. Microporous Mesoporous Mater 219:134–144. https://doi.org/10.1016/J.MICROMESO.2015.08.003

11. Kim S-H, Choi P-P (2017) Enhanced Congo red dye removal from aqueous solutions using iron nanoparticles: adsorption, kinetics, and equilibrium studies. Dalton Trans 46:15470–15479. https://doi.org/10.1039/C7DT02076G

12. Grassian VH (2005) Environmental catalysis. Taylor & Francis, Milton Park

13. Rothenberg G (2017) Catalysis: concepts and green applications. Wiley, Incorporated

14. Corma A, García H, Llabrés i Xamena FX (2010) Engineering metal organic frameworks for heterogeneous catalysis. Chem Rev 110:4606–4655. https://doi.org/10.1021/cr9003924

15. Kuppler RJ, Timmons DJ, Fang Q-R et al (2009) Potential applications of metal–organic frameworks. Coord Chem Rev 253:3042–3066. https://doi.org/10.1016/J.CCR.2009.05.019

16. Rowsell JLC, Yaghi OM (2004) Metal–organic frameworks: a new class of porous materials. Microporous Mesoporous Mater 73:3–14. https://doi.org/10.1016/J.MICROMESO.2004.03.034

17. Gangu KK, Maddila S, Mukkamala SB, Jonnalagadda SB (2016) A review on contemporary metal–organic framework materials. Inorg Chim Acta 446:61–74. https://doi.org/10.1016/J.ICA.2016.02.062

18. Wang F, Wang C, Yu Z et al (2016) Two multifunctional Mn(II) metal–organic frameworks: synthesis, structures and applications as photocatalysis and luminescent sensor. Polyhedron 105:49–55. https://doi.org/10.1016/J.POLY.2015.11.043

19. Czaja AU, Trukhan N, Müller U (2009) Industrial applications of metal–organic frameworks. Chem Soc Rev 38:1284. https://doi.org/10.1039/b804680h

20. de Miguel M, Ragon F, Devic T et al (2012) Evidence of photoinduced charge separation in the metal–organic framework

MIL-125(Ti)–NH $_2$. ChemPhysChem 13:3651–3654. https://doi.org/10.1002/cphc.201200411

21. Alvaro M, Carbonell E, Ferrer B et al (2007) Semiconductor behavior of a metal–organic framework (MOF). Chem A Eur J 13:5106–5112. https://doi.org/10.1002/chem.200601003

22. Passalacqua R, Perathoner S, Centi G (2017) Semiconductor, molecular and hybrid systems for photoelectrochemical solar fuel production. J Energy Chem 26:219–240. https://doi.org/10.1016/J.JECHEM.2017.03.004

23. Wen M, Mori K, Kuwahara Y et al (2017) Design and architecture of metal organic frameworks for visible light enhanced hydrogen production. Appl Catal B Environ 218:555–569. https://doi.org/10.1016/J.APCATB.2017.06.082

24. Kumar P, Vellingiri K, Kim K-H et al (2017) Modern progress in metal–organic frameworks and their composites for diverse applications. Microporous Mesoporous Mater 253:251–265. https://doi.org/10.1016/J.MICROMESO.2017.07.003

25. Zhu J, Maza WA, Morris AJ (2017) Light-harvesting and energy transfer in ruthenium(II)-polypyridyl doped zirconium(IV) metal–organic frameworks: a look toward solar cell applications. J Photochem Photobiol A Chem 344:64–77. https://doi.org/10.1016/J.JPHOTOCHEM.2017.04.025

26. Su Y, Zhang Z, Liu H, Wang Y (2017) Cd0.2Zn0.8S@UiO-66-NH $_2$ nanocomposites as efficient and stable visible-light-driven photocatalyst for H $_2$ evolution and CO $_2$ reduction. Appl Catal B Environ 200:448–457. https://doi.org/10.1016/J.APCATB.2016.07.032

27. Cui J-W, Hou S-X, Li Y-H, Cui G-H (2017) A multifunctional Ni(ii) coordination polymer: synthesis, crystal structure and applications as a luminescent sensor, electrochemical probe, and photocatalyst. Dalton Trans 46:16911–16924. https://doi.org/10.1039/C7DT03874G

28. Kang W-C, Li Y-H, Qin Z-B, Cui G-H (2018) Synthesis, structures and characterization of two cobalt(II) coordination polymers with 2,5-dichloroterephthalic acid and flexible bis(benzimidazole) ligands. Transit Met Chem. https://doi.org/10.1007/s11243-018-0242-4

29. Li J-X, Qin Z-B, Li Y-H, Cui G-H (2018) Sonochemical synthesis and properties of two new nanostructured silver(I) coordination polymers. Ultrason Sonochem 48:127–135. https://doi.org/10.1016/J.ULTSONCH.2018.05.016

30. Du J-J, Yuan Y-P, Sun J-X et al (2011) New photocatalysts based on MIL-53 metal–organic frameworks for the decolorization of methylene blue dye. J Hazard Mater 190:945–951. https://doi.org/10.1016/J.JHAZMAT.2011.04.029

31. Zhao H, Xia Q, Xing H et al (2017) Construction of pillared-layer MOF as efficient visible-light photocatalysts for aqueous Cr(VI) reduction and dye degradation. ACS Sustain Chem Eng 5:4449–4456. https://doi.org/10.1021/acssuschemeng.7b00641

32. Guesh K, Caiuby CAD, Mayoral Á et al (2017) Sustainable preparation of MIL-100(Fe) and its photocatalytic behavior in the degradation of methyl orange in water. Cryst Growth Des 17:1806–1813. https://doi.org/10.1021/acs.cgd.6b01776

33. Zhu J, Li P-Z, Guo W et al (2018) Titanium-based metal–organic frameworks for photocatalytic applications. Coord Chem Rev 359:80–101. https://doi.org/10.1016/J.CCR.2017.12.013

34. Alver E, Bulut M, Metin AÜ, Çiftçi H (2017) One step effective removal of Congo Red in chitosan nanoparticles by encapsulation. Spectrochim Acta Part A Mol Biomol Spectrosc 171:132–138. https://doi.org/10.1016/J.SAA.2016.07.046

35. Ma C, Wang F, Zhang C et al (2017) Photocatalytic decomposition of Congo red under visible light irradiation using MgZnCr–TiO $_2$ layered double hydroxide. Chemosphere 168:80–90. https://doi.org/10.1016/J.CHEMOSPHERE.2016.10.063

36. Wang H, Yuan X, Wu Y et al (2015) Facile synthesis of amino-functionalized titanium metal–organic frameworks and their superior visible-light photocatalytic activity for Cr(VI) reduction. J Hazard Mater 286:187–194. https://doi.org/10.1016/J.JHAZMAT.2014.11.039

37. Lowell S, Lowell S (2004) Characterization of porous solids and powders: surface area, pore size, and density. Kluwer Academic Publishers, Berlin

38. Thommes M, Cychosz KA (2014) Physical adsorption characterization of nanoporous materials: progress and challenges. Adsorption 20:233–250. https://doi.org/10.1007/s10450-014-9606-z

39. Thommes M (2016) Physisorption of gases, with special reference to the evaluation of surface area and pore size distribution (IUPAC Technical Report). Chem Int 38:25. https://doi.org/10.1515/ci-2016-0119

40. Vargas WE, Niklasson GA (1997) Applicability conditions of the Kubelka–Munk theory. Appl Opt 36:5580. https://doi.org/10.1364/AO.36.005580

41. Essick JM, Mather RT (1993) Characterization of a bulk semiconductor's band gap via a near-absorption edge optical transmission experiment. Am J Phys 61:646–649. https://doi.org/10.1119/1.17173

42. Vermoortele F, Maes M, Moghadam PZ et al (2011) P-xylene-selective metal–organic frameworks: a case of topology-directed selectivity. J Am Chem Soc 133:18526–18529. https://doi.org/10.1021/ja207287h

43. Dan-Hardi M, Serre C, Frot T et al (2009) A new photoactive crystalline highly porous titanium(IV) dicarboxylate. J Am Chem Soc 131:10857–10859. https://doi.org/10.1021/ja903726m

44. Fu Y, Sun D, Chen Y et al (2012) An amine-functionalized titanium metal–organic framework photocatalyst with visible-light-induced activity for CO $_2$ reduction. Angew Chemie Int Ed 51:3364–3367. https://doi.org/10.1002/anie.201108357

45. Hatchard CG, Parker CA (1956) A new sensitive chemical actinometer. II. Potassium ferrioxalate as a standard chemical actinometer. Proc R Soc A Math Phys Eng Sci 235:518–536. https://doi.org/10.1098/rspa.1956.0102

46. Harris GD, Dean Adams V, Moore WM, Sorensen DL (1987) Potassium ferrioxalate as chemical actinometer in ultraviolet reactors. J Environ Eng 113:612–627. https://doi.org/10.1061/(ASCE)0733-9372(1987)113:3(612)

47. Hirakawa T, Nosaka Y (2002) Properties of O_2^- and OH $^.$ formed in TiO $_2$ aqueous suspensions by photocatalytic reaction and the influence of H $_2$O $_2$ and some ions. Langmuir 18:3247–3254. https://doi.org/10.1021/la015685a

48. Granados-Oliveros G, Páez-Mozo EA, Ortega FM et al (2009) Degradation of atrazine using metalloporphyrins supported on TiO $_2$ under visible light irradiation. Appl Catal B Environ 89:448–454. https://doi.org/10.1016/J.APCATB.2009.01.001

49. Szychliński J, Bilski P, Martuszewski K, Błażejowski J (1989) Complementary study on the use of the potassium Reinecke's salt as a chemical actinometer. Analyst 114:739–741. https://doi.org/10.1039/AN9891400739

50. McKinstry C, Cathcart RJ, Cussen EJ et al (2016) Scalable continuous solvothermal synthesis of metal organic framework (MOF-5) crystals. Chem Eng J 285:718–725. https://doi.org/10.1016/J.CEJ.2015.10.023

51. Bellamy L (1963) Infrared spectra of complex Molecules. Springer, Netherlands

52. Gomes Silva C, Luz I, Llabrés i Xamena FX et al (2010) Water stable Zr-Benzenedicarboxylate metal–organic frameworks as photocatalysts for hydrogen generation. Chem A Eur J 16:11133–11138. https://doi.org/10.1002/chem.200903526

53. Yang L, Kruse B (2004) Revised Kubelka–Munk theory I theory and application. J Opt Soc Am A 21:1933. https://doi.org/10.1364/JOSAA.21.001933

54. Nowak M, Kauch B, Szperlich P (2009) Determination of energy band gap of nanocrystalline SbSI using diffuse reflectance spectroscopy. Rev Sci Instrum 80:046107. https://doi.org/10.1063/1.3103603

55. Jahan F, Islam MH, Smith BE (1995) Band gap and refractive index determination of Mo-black coatings using several techniques. Sol Energy Mater Sol Cells 37:283–293. https://doi.org/10.1016/0927-0248(95)00021-6

56. Lin H, Huang CP, Li W et al (2006) Size dependency of nanocrystalline TiO_2 on its optical property and photocatalytic reactivity exemplified by 2-chlorophenol. Appl Catal B Environ 68:1–11. https://doi.org/10.1016/J.APCATB.2006.07.018

57. Ghosal R, Smith DM (1996) Micropore characterization using the Dubinin–Astakhov equation to analyze high pressure CO_2 (273 K) adsorption data. J Porous Mater 3:247–255. https://doi.org/10.1007/BF01137914

58. Gil A, Grange P (1996) Application of the Dubinin–Radushkevich and Dubinin–Astakhov equations in the characterization of microporous solids. Colloids Surf A Physicochem Eng Asp 113:39–50. https://doi.org/10.1016/0927-7757(96)81455-5

59. Navarro Amador R, Carboni M, Meyer D (2016) Photosensitive titanium and zirconium metal organic frameworks: current research and future possibilities. Mater Lett 166:327–338. https://doi.org/10.1016/J.MATLET.2015.12.023

60. Li Y, Li X, Li J, Yin J (2006) Photocatalytic degradation of methyl orange by TiO_2-coated activated carbon and kinetic study. Water Res 40:1119–1126. https://doi.org/10.1016/J.WATRES.2005.12.042

61. Huang Y-B, Liang J, Wang X-S, Cao R (2017) Multifunctional metal–organic framework catalysts: synergistic catalysis and tandem reactions. Chem Soc Rev 46:126–157. https://doi.org/10.1039/C6CS00250A

62. Izumi I, Fan F-RF, Bard AJ (1981) Heterogeneous photocatalytic decomposition of benzoic acid and adipic acid on platinized titanium dioxide powder. The photo-Kolbe decarboxylative route to the breakdown of the benzene ring and to the production of butane. J Phys Chem 85:218–223. https://doi.org/10.1021/j150603a002

63. Wei T-Y, Wan C (1992) Kinetics of photocatalytic oxidation of phenol on TiO_2 surface. J Photochem Photobiol A Chem 69:241–249. https://doi.org/10.1016/1010-6030(92)85284-2

64. Pichat P, Guillard C, Amalric L et al (1995) Assessment of the importance of the role of H_2O_2 and O_2o- in the photocatalytic degradation of 1,2-dimethoxybenzene. Sol Energy Mater Sol Cells 38:391–399. https://doi.org/10.1016/0927-0248(94)00231-2

65. Granados-Oliveros G, Torres E, Zambrano M et al (2018) Formation of hydroxyl radicals by α-Fe_2O_3 microcrystals and its role in photodegradation of 2,4-dinitrophenol and lipid peroxidation. Res Chem Intermed 44:3407–3424. https://doi.org/10.1007/s11164-018-3315-2